

# Scalable Double Regularization for 3D Nano-CT Reconstruction

Wei Tang<sup>a,b</sup>, Mengt Li<sup>b,\*</sup>

<sup>a</sup>*Institute of Geology and Geophysics, Chinese Academy of Science, No. 19, Beitucheng Western Road, Chaoyang District, Beijing, China*

<sup>b</sup>*Department of Statistics, Rice University, 6100 Main Street, MS 138, Houston, TX*

---

## Abstract

Nano-CT (computerized tomography) has emerged as a non-destructive high-resolution cross-sectional imaging technique to effectively study the sub- $\mu\text{m}$  pore structure of shale, which is of fundamental importance to the evaluation and development of shale oil and gas. Nano-CT poses unique challenges to the inverse problem of reconstructing the 3D structure due to the lower signal-to-noise ratio (than Micro-CT) at the nano-scale, increasing sensitive to the misaligned geometry caused by the movement of object manipulator, limited sample size, and a larger volume of data at higher resolution. In this paper, we propose a scalable double regularization (SDR) method to utilize the entire dataset for simultaneous 3D structural reconstruction across slices through total variation regularization within slices and  $L_1$  regularization between adjacent slices. SDR allows information borrowing both within and between slices, contrasting with the traditional methods that usually build on slice by slice reconstruction. We develop a scalable and memory-efficient algorithm by exploiting the systematic sparsity and consistent geometry induced by such Nano-CT data. We illustrate the proposed method by simulation and a real data application using shale rocks acquired in the Sichuan Basin.

**Keywords:** Shale, Nano-CT, Image reconstruction, Regularization, Scalable algorithm

---



---

\*Corresponding author

## 1. Introduction

Nano-CT is an emerging imaging technique that provides a much higher spatial resolution than its precedent Micro-CT, and has been widely used in many fields such as material science [1], biomedicine [2], and chemical application [3]. In the area of geoscience, X-ray Nano-CT has attracted growing interests in shale gas and oil to effectively study the structure of shale that has abundant interior pores at the nano-scale, understanding which is a crucial step in the exploration of shale gas. High quality image reconstruction in Nano-CT with less artifacts and sharper edges is a crucial step for subsequent analysis (for example, image segmentation [4]), and thus plays an instrumental role in quantitatively analyzing different components such as organic matter, pores, and brittle minerals. However, the enhanced spatial resolution in Nano-CT poses unique challenges to the inverse problem of reconstructing the 3D structure due to the lower signal-to-noise ratio (than Micro-CT) at the nano-scale, increasing sensitive to the misaligned geometry caused by the movement of object manipulator, limited sample size, and a larger volume of data at higher resolution.

Most of the existing methods for CT reconstruction at various scales view the 3D input slice by slice, which might perform well at a high signal-to-noise ratio. While synchrotron radiation makes it possible to reconstruct shale structures at the nano-scale, the noise level in Nano-CT is often inevitably heavier than in Micro-CT or industry-CT, partly due to the geometrical deviation [5] and observation system [6] in use. Since the size of Charge Coupled Device (CCD) is much smaller than regular CT devices, the number of projection angles is orders of magnitude smaller than Micro-CT. One motivation of this paper is to utilize the entire data set in CT reconstruction to allow information borrowing within slices as well as between slices, while addressing the daunting memory and computation issues caused by the large volume of data at high spatial resolution.

We propose a scalable double regularization (SDR) method to utilize the entire data set for simultaneous 3D structural reconstruction through total vari-

ation regularization within slices and  $L_1$  regularization between adjacent slices. This strategy improves upon the traditional methods that build on slice by slice reconstruction at a low signal-to-noise ratio. The proposed SDR method is well suited for a "blank edge" problem in the projection data of Nano-CT. We develop a scalable and memory-efficient algorithm for routine implementation. The key idea is to exploit the systematic sparsity and some inherent geometry induced by Nano-CT data, without which even loading the data into memory is challenging. Experimental results using simulation and a real data application using shale rocks acquired in the Sichuan Basin show that the proposed SDR often outperforms existing methods both quantitatively and qualitatively. For shale oil and gas, improved reconstruction by SDR is expected to increase the accuracy in analyzing the elementary volume and statistical characteristics of pore sizes, as a result of the sharper edges and less noisy artifacts when recovering vital pore structures. The proposed method is generic and can be applied to other fields using Nano-CT.

## 2. Related work

There has been a rich literature in CT reconstruction since CT was introduced in 1973 [7]. Most of the existing methods attempt to inverse a function through its projections recorded at a series of angles. Two main classes of methods include analytic methods such as filtered back projection (FBP) and iterative methods such as algebraic reconstruction technique (ART). Methods based on deep learning have been recently developed to build connections between low-dose CT images and routine-dose CT images through large training data.

*Filtered back projection (FBP).* FBP remains one of the most popular methods in the software of CT devices [8]. FBP uses analytical explicit solution and is based on the Fourier Slice Theorem. Consider a 2D object (such as one slice in a 3D object), projection from each angle gives the value of the object's two-dimensional Fourier transform along a single line. Since directly back projection

will blur the final image, we alter the projection data by a high-pass filter or a sharpening filter which can pick up sharp edges within the projection. Then the final step is backprojection, in which we add together the two-dimensional inverse Fourier transform of each filtered projection [9]. By using the Fast Fourier Transform (FFT) algorithm, the implementation of FBP is very fast. However, FBP does not provide much flexibility to allow the incorporation of prior information on the structure or a model-based approach rooting in the imaging physics [10].

*Iterative reconstruction (IR) reconstruction methods..* IR methods are a flexible alternative to iteratively improve the reconstruction in the data space, and have been developed rapidly. Although they always demand more computational power, IR methods usually generate less artifacts than FBP. IR encompasses a variety of methods in the literature from an algebraic perspective such as algebraic reconstruction technique (ART) [11], simultaneous ART [12], simultaneous iterative reconstruction technique (SIRT) [13], ordered subset simultaneous iterative reconstruction technique (OSSIRT) [14], multiplicative ART [15], iterative coordinate descent [16]. Another line of IR methods is from a statistical perspective such as maximum likelihood expectation-maximization [17] and ordered subset expectation-maximization [18]. As an ill-posed problem, CT reconstruction has attracted numerous developments using various regularization to incorporate constraints in the reconstruction [19, 20, 21, 22, 23, 24, 25, 26, 27, 16, 28, 29, 30].

*Learning-based methods..* There has been a surge of interest to develop deep learning-based techniques for a variety of tasks in CT reconstruction [31]. These include using routine CT images to train a neural network to enhance the spatial resolution aiming at the so-called *super-resolution* [32, 33], improving image quality by denoising [34, 35], reducing the number of projections needed [36], and mapping projection data collected from multi-energy source to monochromatic projection data [37], just to name a few. Learning-based methods have lead

to numerous promising results, especially when data are sampled at limited number of angles as in medical and biological imaging.

Most of the methods mentioned above are motivated by and applied to medical CT, where a typical spatial resolution is around  $500\mu\text{m}$  [38] and the radiation dose on the sample as well as the uncertainty caused by multi-energy source is always a big concern. In contrast, a synchrotron-based source which is well known for high brilliance, high stability, and high flux, can achieve a super spatial resolution up to nm scale [6]. Moreover, if the sample is rock, it is much less a concern of a high dose in the imaging process than for biological samples. In practice, it is often not realistic to find large training images at the nano-scale to train a neural network for a specific rock task. As far as we know, there is no literature to apply deep learning-based methods for Nano-CT. When the noise level is high, borrowing information from neighboring slices has the potential to improve the accuracy of the reconstructed objects.

Next we propose a new method that is well suited for Nano-CT reconstruction, starting with an introduction to the basic theory of CT and the motivation of the method.

### 3. Methods

#### 3.1. Background: Theory and Geometry of CT

CT creates an image using X-ray flux measurements from different angles. If the input X-ray photons are mono-energetic, the X-ray intensities passing the object follow the Beer-Lambert Law:

$$\Delta I/I = f(x, y)\Delta r, \quad (1)$$

where  $f(x, y)$  is the linear attenuation coefficient of the object (also called the absorbing function),  $\Delta r$  is the small distance that the ray travels, and the  $\Delta I$  is the attenuation of energy. Let  $I_0$  and  $I_1$  be the intensity of the beam entering and exiting the object, respectively, and  $\mathcal{L}$  be the path that the X-ray travels.

Then Equation (1) yields

$$I_1/I_0 = \exp \left\{ - \int_{\mathcal{L}} f(x, y) dr \right\}. \quad (2)$$

The integral in Equation (2) can be regarded as a mapping from  $\mathbb{R}^2$  to the set of its line integral, which can be further expressed as the so-called Radon transform. Therefore, the main task to estimate the linear attenuation coefficient function  $f$ , which describes the object's structure, amounts to the inversion of the Radon transform in  $\mathbb{R}^2$ .

Synchrotron radiation contains complex devices like collimating mirror and toroidal mirror which will provide a hollow cone illumination on the sample [39]. Taking the size of the sample into consideration, the scanning geometries can be treated as parallel beam: The parallel light comes from one side of the object and the detector on the other side get the optical signal by CCD. Iterative reconstruction methods assume the linear attenuation  $f(x, y)$  is composed by square grids and in each grid  $f(x, y)$  is constant. Suppose we discretize the linear attenuation of the 3D object to an  $L \times L \times L$  array, and let  $\mathbf{f}^l$  be the  $l$ th slice where  $l = 1, \dots, L$  from top to bottom of the object. Let  $\Theta$  be the set of all projection angles, and  $\mathbf{p}_\theta$  be the projection of the object when the object is rotated by  $\theta \in \Theta$ . Collecting the  $l$ th row of every  $\mathbf{p}_\theta$  leads to the projection of the  $l$ th slice, denoted by  $\mathbf{p}^l$ . See Figure 1 for a demonstration of the introduced notation and the inverse Radon transform mapping each  $\mathbf{p}^l$  to  $\mathbf{f}^l$ . Note that we use the logarithmic scale for all projections  $\mathbf{p}^l$  in this paper.

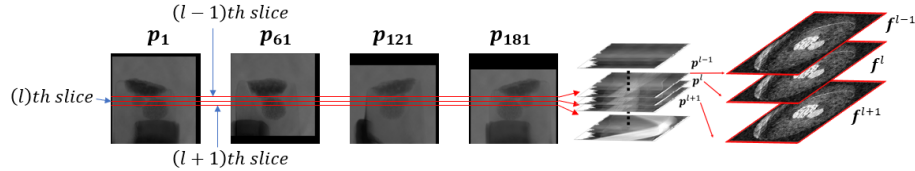


Figure 1: Demonstration of the image acquiring process in Nano-CT.

Throughout the paper, we stack  $\mathbf{f}^l$  and  $\mathbf{p}^l$  column by column into a vector of length  $L^2$  and length  $L \times |\Theta|$ , respectively. Equation (2) leads to the following

model

$$p_i^l = \sum_{j=1}^{L^2} W_{ij} f_j^l + \varepsilon_i^l, \quad \text{or in matrix form, } \mathbf{p}^l = \mathbf{W} \mathbf{f}^l + \boldsymbol{\varepsilon}^l, \quad (3)$$

where  $f_j^l$  is the  $j$ th grid in the  $l$ th slice  $\mathbf{f}^l$ ,  $p_i^l$  the acquired projection data of the  $l$ th slice from the  $i$ th ray, and  $\varepsilon_i^l$  is random noise at the  $l$ th slice. Here  $W_{ij}$  is the contribution of the  $j$ th pixel to the  $i$ th ray; for example, if we use a simple project structure,  $W_{ij}$  is the intersection length of the  $i$ th ray and the  $j$ th pixel. In general, each row of  $\mathbf{W}$  correspond to one ray and each column of  $\mathbf{W}$  corresponds to one pixel.

### 3.2. Motivation: sparsity and blank edge

In this section, we motivate our methods using shale samples from the Sichuan Basin, mined from approximately 2756 m in depth and formed in a marine sedimentary environment. Samples are milled to cylinder to produce 181 image frames taken with the azimuth angle rotating from  $-89^\circ$  to  $+90^\circ$  at pixel size 50nm; see Section 4.1 for detailed descriptions of this dataset.

We apply the FBP algorithm to 180 sequential image frames. The field of view in Nano-CT should be composed of a few pores and high-density material. Their absorption coefficient to light varies greatly. It is expected that the difference between adjacent slices should be mostly zero but contain edges of the structure, i.e., sparse. Figure 2 shows the difference of selected adjacent slices after reconstruction along with the histograms of the intensity, which clearly confirms the sparsity pattern. A slice by slice algorithm such as FBP does not enforce sparse differences, and to incorporate such constraints into the reconstruction procedure is expected to improve accuracy and sharpness of edges.

Another motivation is that there are blank edges in the raw projection data. Blank edges are more often in Nano-CT because even a tiny movement of the object becomes significant compared to CT at coarser scales (such as nm). The cartoon in the left plot of Figure 3 demonstrates that if the object manipulator moves up a little, the bottom of the projection data cannot be recorded. The

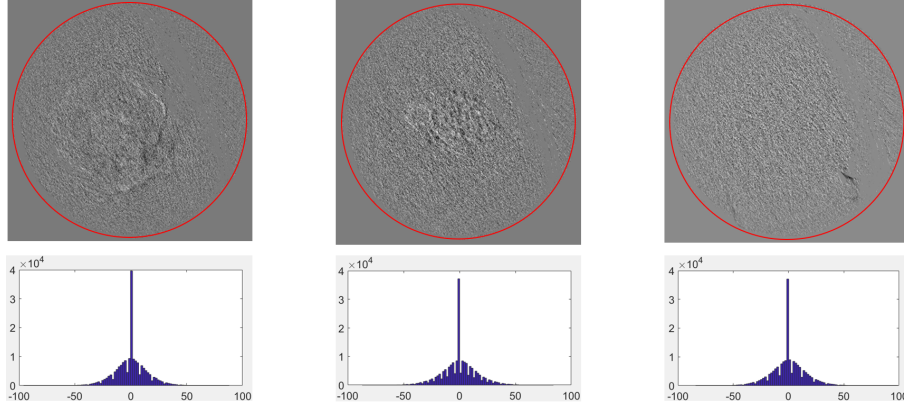


Figure 2: The difference between two adjacent slices given by FBP by subtracting the  $l$  slice from the  $l + 1$ th slice. The three columns correspond to  $l = 200, 300, 400$ , left to right. The second row is the corresponding histogram of intensities within the red circle.

same phenomenon happens when the object manipulator moves left or right. The vibration changes irregularly with the angle so most of the projection  $\mathbf{p}_\theta$  will lose some data on edge after the geometric correction. The right plot of Figure 3 shows such an effect using one slice from our observed real data.

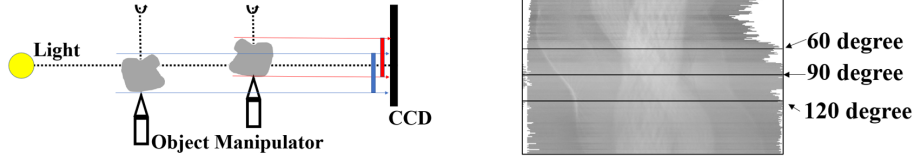


Figure 3: geometric deviation and projection of 280th slice corrupted by blank edges

FBP and traditional IR methods essentially assume uniform sampling without considering blank edges in the reconstruction. Moreover, the adjacent projections  $\mathbf{p}^l$  in middle slices (which contain the most useful information about the object) have identical blank edges, according to the device setup in image acquiring. This systematic geometry strongly supports information borrowing across slices, as a simultaneous reconstruction across slices should alleviate the missing data issue of blank edges.



### 3.3. Scalable Double Regularization (SDR)

Existing methods in Section 3.1 reconstruct the structure slice by slice, which might perform well at high signal-to-noise ratio. However, low signal-to-noise ratio is expected for Nano-CT due to the high resolution in the imaging process and lower photon density [6]. In addition, scalability and memory efficiency become crucial at high resolution. We propose a scalable double regularization (SDR) approach to reconstruct the 3D Nano-CT structure:

$$(\hat{\mathbf{f}}^1, \dots, \hat{\mathbf{f}}^L) = \arg \min_{\mathbf{f}^1, \dots, \mathbf{f}^L} \sum_{l=1}^L \|\mathbf{p}^l - \mathbf{W} \mathbf{f}^l\|_2 + \lambda_1 \sum_{l=1}^L g_1(\mathbf{f}^l) + \lambda_2 g_2(\mathbf{f}^1, \dots, \mathbf{f}^L), \quad (4)$$

where  $g_1$  and  $g_2$  are the regularization terms to control the within-slice and between-slice variation, respectively. In particular, we use the total variation regularization for  $g_1(\cdot)$ :

$$g_1(\mathbf{f}) =: \|\mathbf{f}\|_{TV} = \sum_{x,y} \|\nabla f_{x,y}\|_2 = \sum_{x,y} \sqrt{(f_{x,y} - f_{x-1,y})^2 + (f_{x,y} - f_{x,y-1})^2}, \quad (5)$$

where  $\|\nabla f_{x,y}\|_2$  is the Euclidean norm of the image gradient  $\nabla f_{x,y}$  at  $(x, y)$ . We use the  $L_1$  norm of the different images between neighboring slices for  $g_2$ , i.e.,  $g_2(\mathbf{f}^1, \dots, \mathbf{f}^L) = \sum_{l=1}^{L-1} \|\mathbf{f}^l - \mathbf{f}^{l+1}\|_1$  to favor sparsity between adjacent slices, but note that other forms involving multiple neighboring slices are also applicable. In addition to favor the sparsity constraint in view of the motivation in Section 3.2,  $g_2$  allows information borrowing across slices to utilize the entire dataset for the reconstruction of individual slices, which is critical for Nano-CT reconstruction where the signal-to-noise ratio is much lower than the traditional CT images.

We solve the optimization problem in (4) by building upon the gradient descent approach in TV regularization and coordinate descent for lasso [40], which consists of the following steps.

*Step 1. lasso using contrasts of projections..* We first optimize (4) focusing on the lasso regularization  $g_2$ , and address the TV regularization  $g_1$  in the next step. Using the linearity in Model (3), we take the difference of projections

$\mathbf{p}^{l,l+1} = \mathbf{p}^{l+1} - \mathbf{p}^l$  as input and recast the optimization into a lasso problem:

$$\hat{\mathbf{f}}^{l,l+1} = \arg \min_{\mathbf{f}} \frac{1}{2} \|\mathbf{W}\mathbf{f} - \mathbf{p}^{l,l+1}\|_2 + \lambda_2 \|\mathbf{f}\|_1, \quad (6)$$

where  $\hat{\mathbf{f}}^{l,l+1}$  is an estimate of  $\mathbf{f}^{l,l+1} = \mathbf{f}^{l+1} - \mathbf{f}^l$ . One can generalize this approach for more general forms of  $g_2$  involving higher-order differences of neighboring slices through *contrasts* of projections; here a contrast is a vector  $(c_1, \dots, c_t)$  satisfying that  $c_1 + \dots + c_t = 0$  and  $c_1^2 + \dots + c_t^2 = 1$ .

We adopt the strategy by [41], and update the  $j$ th variable of  $\mathbf{f}$  by

$$\hat{f}_j \leftarrow S \left( \frac{1}{L \times |\Theta|} \sum_{i=1}^{L \times |\Theta|} W_{ij} \left( p_i^{l,l+1} - \sum_{k \neq j}^{L^2} W_{ik} \hat{f}_k \right), \lambda_2 \right), \quad (7)$$

where  $S(\zeta, \eta)$  is the soft-thresholding operator given by

$$S(\zeta, \eta) = \begin{cases} \zeta - \eta & \text{if } \zeta > 0 \text{ and } \eta < |\zeta|, \\ \zeta + \eta & \text{if } \zeta < 0 \text{ and } \eta < |\zeta|, \\ 0 & \text{otherwise.} \end{cases} \quad (8)$$

At given  $\lambda_2$ , we use zero as the initial values and estimate  $\hat{\mathbf{f}}^{l,l+1}$  iteratively until convergence. The selection of  $\lambda_2$  can be carried out through cross-validation, or using initial slice by slice methods to provide a reasonable choice.

*Step 2. TV regularization..* Based on the estimates of the differences of slices, we then use a gradient decent approach in TV regularization reconstructs the 3D object. To this end, we need to calculate the gradient of  $\|\mathbf{f}\|_{TV}$ , which is approximated by

$$\begin{aligned} \frac{\partial \|\mathbf{f}\|_{TV}}{\partial f_{x,y}} &\approx \frac{(f_{x,y} - f_{x-1,y}) + (f_{x,y} - f_{x,y-1})}{\sqrt{\epsilon + \|\nabla f_{x,y}\|_2}} \\ &\quad - \frac{f_{x+1,y} - f_{x,y}}{\sqrt{\epsilon + \|\nabla f_{x+1,y}\|_2}} - \frac{f_{x+1,y} - f_{x,y}}{\sqrt{\epsilon + \|\nabla f_{x,y+1}\|_2}} \end{aligned} \quad (9)$$

where  $\epsilon$  is a small positive number to ensure numerical stability [42], we use Barzilai-Borwein (BB) step [43] to calculate the step size. We use the Kaczmarz

method to choose the initial values, i.e.,

$$\mathbf{f} \leftarrow \mathbf{f} - \frac{\alpha \{\langle \mathbf{f}, \mathbf{W}_i \rangle - p_i\} \mathbf{W}_i}{\|\mathbf{W}_i\|_2^2}, \quad (10)$$

where  $\alpha$  is the relaxation factor and  $\mathbf{W}_i$  is the  $i$ th row of  $\mathbf{W}$ . At each iteration, the reconstruction is updated by combining the construction of slices and differences of slices as follows

$$\hat{\mathbf{f}}^l \leftarrow (\hat{\mathbf{f}}^l + \hat{\mathbf{f}}^{l-1} + \hat{\mathbf{f}}^{l+1} + \hat{\mathbf{f}}^{l,l+1} - \hat{\mathbf{f}}^{l-1,l})/3. \quad (11)$$

The algorithm will terminate when certain convergence criterion is met.

#### 3.4. Scalability and Memory efficiency

For real data with a  $512 \times 512$  resolution and 180 angles of projections, the dimension of  $\mathbf{W}$  is around  $(512 \times 512) \times (512 \times 180) = (2.6 \times 10^5) \times (9.2 \times 10^4) > 2 \times 10^{10}$  pixels, leading to daunting memory and computation issues. A dense matrix with the size of  $\mathbf{W}$  may occupy 180Gb memory, exceeding the maximum memory limit by many workstations. However, in the CT imaging process, one ray can only go through few pixels of the entire image: for a  $m \times n$  matrix  $\mathbf{W}$  only  $\sqrt{n}$  of each row of  $\mathbf{W}$  is non-zero. We exploit this extreme sparsity to store  $\mathbf{W}$ 's efficiently by only storing the non-zero values and their locations, which dramatically reduces the memory demand. For example, we only need less than 1.75Gb memory using the example above.

The sparse structure of  $\mathbf{W}$  not only provide efficient memory allocation for the output, but also improve the computation by taking advantage of efficient sparse matrix operations. The process of solving Equation (10) and lasso requires calculating many inner products between  $\mathbf{W}$  and other vectors. In the solvers for the TV and lasso regularization, the utilization of sparsity reduces the complexity of each inner product operation from  $O(n)$  to  $O(\sqrt{n})$ .

The Matlab code to implement the proposed methods with demonstration is available at <https://github.com/xylimeng/SDR-CT>.

## 4. Experiments

### 4.1. Synthetic data

We use a classic 3D shepp-logan phantom of size  $128 \times 128 \times 128$ . For each slice, we sample equal-spaced points on each ray line. The value of  $f(x, y)$  at any  $(x, y) \in \mathbb{R}$  is determined by bilinear interpolation according to its closest sampled points:

$$f(x, y) \approx \begin{bmatrix} x_{k+1} - x & x - x_k \end{bmatrix} \begin{bmatrix} f(x_k, y_k) & f(x_k, y_{k+1}) \\ f(x_{k+1}, y_k) & f(x_{k+1}, y_{k+1}) \end{bmatrix} \begin{bmatrix} y_{k+1} - y \\ y - y_k \end{bmatrix} \quad (12)$$

In the middle of Figure 4 demonstrates such discretization process to generate  $\mathbf{f}^l$ . We consider three scenarios depending on the standard deviation  $\sigma_{\text{true}}$  of the Gaussian noise added to the true projection: noiseless ( $\sigma_{\text{true}} = 0$ ), low noise ( $\sigma_{\text{true}} = 0.5$ ), and high noise ( $\sigma_{\text{true}} = 1$ ). In order to mimic the blank edges as in the real data, we randomly remove some pixels of the projection on the edge. The number of pixels removed are the same for three noise level. Right of Figure 4 shows projection of 64th slice corrupted by Gaussian noise ( $\sigma_{\text{true}} = 1$ ) and blank edges. We compare the proposed SDR with FBP, OSSIRT (one of

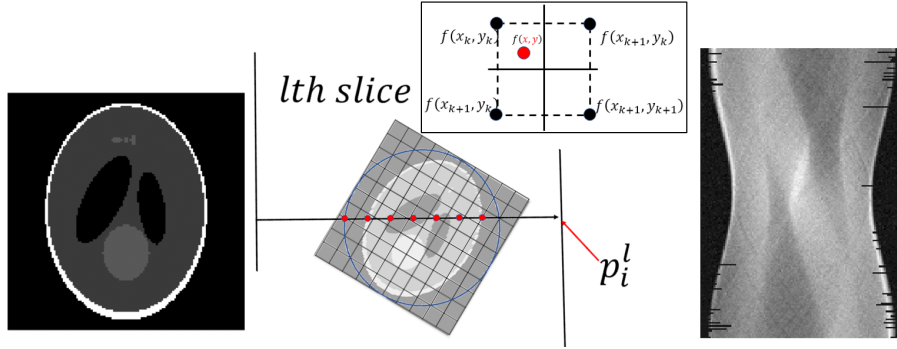


Figure 4: Phantom of 64th slice, Demonstration of generating  $\mathbf{f}^l$  ( $l = 64$ ) via bilinear interpolation, and Simulated projection corrupted by Gaussian noise and blank edges (from left to right).

the best IR methods without regularization [14]), and TVART [19] (one of the best IR methods combined with regularization). We run up 20 iterations of (10)

Table 1: Comparison of different methods using 3D shepp-logan phantom.

Methods	noiseless		low noise		high noise	
	SNR	SSIM	SNR	SSIM	SNR	SSIM
FBP	9.19	0.365	16.92	0.527	15.25	0.434
OSSIRT	8.17	0.448	13.27	0.598	13.06	0.583
TVART	30.26	0.670	29.25	0.646	20.20	0.602
SDR	<b>30.36</b>	<b>0.676</b>	<b>32.28</b>	<b>0.655</b>	<b>26.05</b>	<b>0.612</b>

for all methods to have a fair comparison. The relaxation factor  $\alpha$  was set to 1 in Equation (10),  $\lambda_2$  was set to 0.02 when solve Equation (6) and  $\lambda_1$  was set to 0.5.

In order to assess the performance of each method, we use the signal-to-noise ratio (SNR) and the structural similarity (SSIM) index [44] between the reconstructed structure  $\hat{f}$  and the true structure  $f$ :

$$\text{SNR} = 10 \log \left( \frac{\sum_{i=1}^{L^2} (f_i - \mu_f)^2}{\sum_{i=1}^{L^2} (\hat{f}_i - f_i)^2} \right), \quad (13)$$

$$\text{SSIM} = \frac{(2\mu_f\mu_{\hat{f}} + C_1)(2\sigma_{f\hat{f}} + C_2)}{(\mu_f^2 + \mu_{\hat{f}}^2 + C_1)(\sigma_f^2 + \sigma_{\hat{f}}^2 + C_2)}, \quad (14)$$

where  $\mu_{\hat{f}}, \mu_f$  are the means of  $\hat{f}$  and  $f$ ,  $\sigma_f, \sigma_{\hat{f}}$  are the standard deviations of  $\hat{f}$  and  $f$ , and  $\sigma_{f\hat{f}}$  is the covariance of  $\hat{f}$  and  $f$ .

Figure 5 shows that there are significant artifacts in the reconstructed images of FBP and OSSIRT in the noiseless case (see the first row), suggesting that they suffer considerably from the blank edge issue. TVART and SDR provide the best visualization consistently across various scenarios, but the proposed SDR tends to give clearer reconstruction at high noise level (3rd row). Since all iterative methods use the same number of iterations, the comparison between OSSIRT (blurred) and SDR (clearer) indicates the advantage of incorporating regularization in the reconstruction.

The 20 slices in the middle contain most of the important structures for the

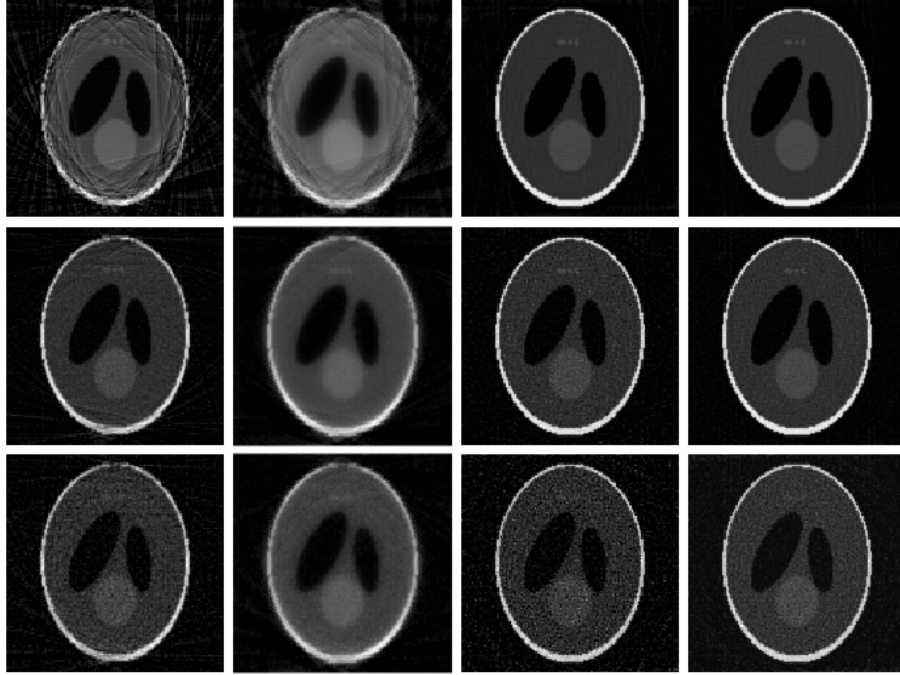


Figure 5: Reconstruction of the 64th slice using FBP, OSSIRT, TVART, and SDR (left to right). The three rows correspond to the cases of noiseless, low noise, and high noise.

3D Shepp-Logan phantom data. Table 1 reports the average objective index performance across these 20 slices for each method. Overall, SDR is uniformly the best method using SNR and SSIM. We can see that SDR tends to give increasingly better summaries at higher noise level, relative to alternatives such as TVART. This suggests SDR might be particularly well suited for our real data application as a high noise level is expected in Nano-CT.

#### 4.2. Real data application

We use W201 shale samples provided by Institute of Geology and Geophysics, Chinese Academy of Sciences [45]. W201 is one key well in Sichuan Basin that produces industrial-scale gas flow and was drilled in 2011 by the China National Petroleum Corporation. Sourced from approximately 2756m in depth, these W201 shale samples had formed in a marine sedimentary environ-

ment, where the lithology mainly consists of dark shale mixed with siltstone and fine sandstone [46]. The Nano-CT experiments were carried out at beamline BL01B, the National Synchrotron Radiation Research Center (NSRRC) in Hsinchu, Taiwan. Samples were milled to cylinder with  $7 - 10\mu m$  in diameter. The Synchrotron Radiation beamline provided 2D micrograph and 3D tomography with pixel size of 50nm, with the first-order diffraction of a Fresnel zone plate at an X-ray energy of 8Kev [47].

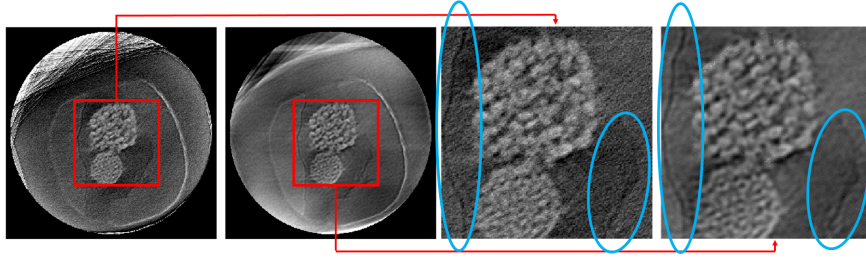


Figure 6: Comparison of SDR and FBP. From left to right is the reconstruction of FBP, SDR, and zoomed plots of the region within the red frame by FBP and SDR. Blue circles in the zoomed plots highlight a long microfracture and a short microfracture.

We compare the two methods, FBP (which is applied by most Nano-CT devices directly) and our algorithm SDR. The visual comparison is shown in Figure 6. We find that the proposed SDR exhibits less noisy artifacts than the FBP reconstruction. In the zoomed plots, framboid pyrite and intercrystalline pores are shown between a "longer microfracture" of dozens of micrometers (the long black line enclosed by the blue circle on the left) and a "shorter microfracture" (enclosed by the blue circle at the right bottom of zoomed plots). The result given by SDR provides a much more clear shorter microfracture than FBP especially in the middle of the shorter microfracture, where visually the reconstructed fracture of FBP is hardly distinguishable from noise. We also calculate a no-reference structural sharpness (NRSS) metric to quantitatively measure the sharpness of the reconstruction:

$$NRSS = \sum_x \sum_y \{(f_{x+1,y} - f_{x,y})^2 + (f_{x,y} - f_{x,y+1})^2\}.$$

Figure 7 compares the NRSS from the 210th slice to the 290th slice, clearly

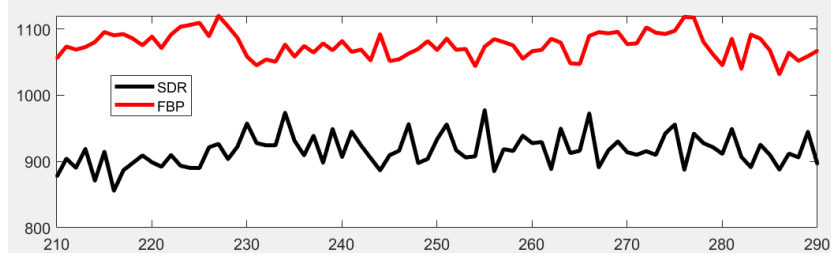


Figure 7: NRSS of SDR vs. FBP from the 210th slice to the 290th slice.

indicating that SDR provides much sharper reconstructions. The enhanced contrast by SDR is expected to improve the subsequent post processing steps such as segmentation. In practice, such improved reconstruction by SDR is expected to increase accuracy in analyzing the elementary volume and statistical characteristics of pore sizes, pyrite and organic matter, partly due to the sharper edges and less noisy reconstructions when recovering vital structures.

## References

## References

- [1] S. Komini Babu, H. Taek Chung, P. Zelenay, S. Litster, Resolving electrode morphologies impact on platinum group metal free cathode performance using nano-ct of 3d hierarchical pore and ionomer distributions, *ACS Applied Materials & Interfaces* 8 (48).
- [2] B. Yu, L. Weber, A. Pacureanu, M. Langer, C. Olivier, P. Cloetens, F. Peyrin, Phase retrieval in 3d x-ray magnified phase nano ct: Imaging bone tissue at the nanoscale, in: *IEEE International Symposium on Biomedical Imaging*, 2017, pp. 56–59. doi:10.1109/ISBI.2017.7950467.
- [3] S. Cagno, D. A. Brede, G. Nuyts, F. Vanmeert, A. Pacureanu, R. Tucoulou, P. Cloetens, G. Falkenberg, K. Janssens, B. Salbu, Combined nano-ct and



nano-xrf imaging of cobalt nanoparticles in *caenorhabditis elegans*, *Analytical Chemistry* 89 (2017) 11435–11442.

- [4] Y. Wang, L. Wang, J. Wang, Z. Jiang, C.-C. Wang, Y. Fu, Y.-F. Song, Y. Wang, D. Liu, C. Jin, Multiscale characterization of three-dimensional pore structures in a shale gas reservoir: A case study of the longmaxi shale in sichuan basin, china, *Journal of Natural Gas Science and Engineering* 66 (2019) 207 – 216. doi:<https://doi.org/10.1016/j.jngse.2019.04.009>.
- [5] A. Sasov, L. Xuan, P. L. Salmon, Compensation of mechanical inaccuracies in micro-ct and nano-ct, *Proceedings of SPIE - The International Society for Optical Engineering* 7078 (2008) 70781C.
- [6] M. Kampschulte, A. C. Langheinrich, J. Sender, H. D. Litzlbauer, U. Althhn, J. D. Schwab, E. Alexandre-Lafont, G. Martels, G. A. Krombach, Nano-computed tomography: Technique and applications, *Rofo Fortschritte Auf Dem Gebiete Der Rontgenstrahlen Und Der Nuklearmedizin* 188 (02) (2016) 146–154.
- [7] L. Mostowycz, R. W. Ware, D. Dochterman, Computerized transverse axial tomography, *Journal of the Kentucky Medical Association* 46 (545) (1973) 128–34.
- [8] X. Pan, E. Y. Sidky, M. Vannier, Why do commercial ct scanners still employ traditional, filtered back-projection for image reconstruction?, *Inverse Problems* 25 (12) (2008) 1230009.
- [9] A. C. Kak, M. Slaney, G. Wang, Principles of computerized tomographic imaging, *Medical Physics* 29 (1) (2002) 49–112.
- [10] G. L. Zeng, Comparison of fbp and iterative algorithms with non-uniform angular sampling, in: *2014 IEEE Nuclear Science Symposium and Medical Imaging Conference (NSS/MIC)*, IEEE, 2014, pp. 1–13.

- [11] R. Gordon, R. Bender, G. T. Herman, Algebraic reconstruction techniques (art) for three-dimensional electron microscopy and x-ray photography, *Journal of Theoretical Biology* 29 (3) (1970) 471–481.
- [12] A. H. Andersen, A. C. Kak, Simultaneous algebraic reconstruction technique (sart): a superior implementation of the art algorithm, *Ultrasonic Imaging* 6 (1) (1984) 81–94.
- [13] P. Gilbert, Iterative methods for the three-dimensional reconstruction of an object from projections., *Journal of Theoretical Biology* 36 (1) (1972) 105–117.
- [14] F. Xu, W. Xu, M. Jones, B. Keszthelyi, J. Sedat, D. Agard, K. Mueller, On the efficiency of iterative ordered subset reconstruction algorithms for acceleration on gpus., *Computer Methods & Programs in Biomedicine* 98 (3) (2010) 261–270.
- [15] C. Badea, R. Gordon, Experiments with the nonlinear and chaotic behaviour of the multiplicative algebraic reconstruction technique (mart) algorithm for computed tomography, *Physics in Medicine & Biology* 49 (8) (2004) 1455–1474.
- [16] J.-B. Thibault, K. D. Sauer, C. A. Bouman, J. Hsieh, A three-dimensional statistical approach to improved image quality for multislice helical ct, *Medical physics* 34 (11) (2007) 4526–4544.
- [17] K. Lange, R. Carson, Em reconstruction algorithms for emission and transmission tomography, *Journal of Computer Assisted Tomography* 8 (2) (1984) 306.
- [18] S. H. Manglos, G. M. Gagne, A. Krol, F. D. Thomas, R. Narayanaswamy, Transmission maximum-likelihood reconstruction with ordered subsets for cone beam ct, *Phys.med.biol* 40 (7) (1995) 1225–1241.

- [19] Z. Chen, X. Jin, L. Li, G. Wang, A limited-angle ct reconstruction method based on anisotropic tv minimization., *Physics in Medicine & Biology* 58 (7) (2013) 2119–41.
- [20] Y. Sun, J. Tao, Image reconstruction from few views by l0-norm optimization, *Chinese Physics B* 23 (7) (2014) 762–766.
- [21] H. Kim, J. Chen, A. Wang, C. Chuang, M. Held, J. Pouliot, Non-local total-variation (nl<sub>tv</sub>) minimization combined with reweighted l1-norm for compressed sensing ct reconstruction, *Physics in Medicine & Biology* 61 (18) (2016) 6878.
- [22] M. Chen, D. Mi, P. He, L. Deng, B. Wei, A ct reconstruction algorithm based on l1/2 regularization, *Computational and Mathematical Methods in Medicine* 2014 (3) (2014) 862910.
- [23] B. Vandeghinste, B. Goossens, R. Van Holen, C. Vanhove, A. Pižurica, S. Vandenberghe, S. Staelens, Iterative ct reconstruction using shearlet-based regularization, *IEEE Transactions on Nuclear Science* 60 (5) (2013) 3305–3317.
- [24] J. Chu, L. Li, Z. Chen, G. Wang, H. Gao, Multi-energy ct reconstruction based on low rank and sparsity with the split-bregman method (mlrss), in: 2012 IEEE Nuclear Science Symposium and Medical Imaging Conference Record (NSS/MIC), IEEE, 2012, pp. 2411–2414.
- [25] X. Jia, B. Dong, Y. Lou, S. B. Jiang, Gpu-based iterative cone-beam ct reconstruction using tight frame regularization, *Physics in Medicine & Biology* 56 (13) (2011) 3787.
- [26] H. Zhang, J. Wang, D. Zeng, X. Tao, J. Ma, Regularization strategies in statistical image reconstruction of low-dose x-ray ct: A review, *Medical Physics* 45 (10) (2018) e886–e907.
- [27] J. Qi, R. M. Leahy, Iterative reconstruction techniques in emission computed tomography, *Physics in Medicine & Biology* 51 (15) (2006) R541.

- [28] X. Zhang, M. Burger, X. Bresson, S. Osher, Bregmanized nonlocal regularization for deconvolution and sparse reconstruction, *SIAM Journal on Imaging Sciences* 3 (3) (2010) 253–276.
- [29] G. Wang, J. Qi, Penalized likelihood pet image reconstruction using patch-based edge-preserving regularization, *IEEE Transactions on Medical Imaging* 31 (12) (2012) 2194–2204.
- [30] T. Bai, X. Mou, Q. Xu, Y. Zhang, Low-dose ct reconstruction based on multiscale dictionary, in: *Medical Imaging 2013: Physics of Medical Imaging*, Vol. 8668, International Society for Optics and Photonics, 2013, p. 86683L.
- [31] T. Higaki, Y. Nakamura, F. Tatsugami, T. Nakaura, K. Awai, Improvement of image quality at ct and mri using deep learning, *Japanese Journal of Radiology* 37 (1) (2019) 73–80.
- [32] K. Umehara, O. J. I. T, Application of super-resolution convolutional neural network for enhancing image resolution in chest ct, *Journal of Digital Imaging* 31 (3) (2017) 1–10.
- [33] J. Park, D. Hwang, K. Y. Kim, S. K. Kang, Y. K. Kim, J. S. Lee, Computed tomography super-resolution using deep convolutional neural network, *Physics in Medicine & Biology* 63 (14) (2018) 145011.
- [34] W. Du, H. Chen, Z. Wu, H. Sun, P. Liao, Y. Zhang, Stacked competitive networks for noise reduction in low-dose ct, *Plos One* 12 (12) (2017) e0190069.
- [35] E. Kang, J. Min, J. C. Ye, A deep convolutional neural network using directional wavelets for low-dose x-ray ct reconstruction, *Medical physics* 44 (10) (2017) e360–e375.
- [36] K. H. Jin, M. T. McCann, E. Froustey, M. Unser, Deep convolutional neural network for inverse problems in imaging, *IEEE Transactions on Image Processing* 26 (9) (2017) 4509–4522.

- [37] W. Cong, G. Wang, Monochromatic ct image reconstruction from current-integrating data via deep learning, arXiv preprint arXiv:1710.03784.
- [38] V. Cnudde, B. Masschaele, M. Dierick, J. Vlassenbroeck, L. Van Hoorebeke, P. Jacobs, Recent progress in x-ray ct as a geosciences tool, *Applied Geochemistry* 21 (5) (2006) 826–832.
- [39] P. Willmott, *An introduction to synchrotron radiation: techniques and applications*, Wiley, 2019.
- [40] R. Tibshirani, Regression shrinkage and selection via the lasso: a retrospective, *Journal of the Royal Statistical Society* 58 (1) (1996) 267–288.
- [41] J. Friedman, T. Hastie, R. Tibshirani, Pathwise coordinate optimization, *Annals of Applied Statistics* 1 (2) (2007) 302–332.
- [42] S. J. Laroque, E. Y. Sidky, X. Pan, Accurate image reconstruction from few-view and limited-angle data in diffraction tomography., *Journal of the Optical Society of America A Optics Image Science & Vision* 25 (7) (2008) 1772–82.
- [43] J. Barzilai, J. M. Borwein, Two-point step size gradient methods, *IMA Journal of Numerical Analysis* 8 (1) (1988) 141–148.
- [44] Z. Wang, E. Simoncelli, A. Bovik, Multiscale structural similarity for image quality assessment, in: *Proc IEEE Asilomar Conference on Signals*, Vol. 2, 2003, pp. 1398 – 1402 Vol.2. doi:10.1109/ACSSC.2003.1292216.
- [45] Y. Wang, J. Pu, L. Wang, J. Wang, Z. Jiang, Y.-F. Song, C.-C. Wang, Y. Wang, C. Jin, Characterization of typical 3d pore networks of jiulaodong formation shale using nano-transmission x-ray microscopy, *Fuel* 170 (2016) 84–91.
- [46] Z. Chen, Shale gas exploration in jiulaodong formation of lower cambrian, sichuan basin, *China Petroleum Exploration* 17 (5) (2012) 71–78.

- [47] Y. F. Song, C. H. Chang, C. Y. Liu, S. H. Chang, U. S. Jeng, Y. H. Lai, D. G. Liu, S. C. Chung, K. L. Tsang, G. C. Yin, X-ray beamlines for structural studies at the nsrrc superconducting wavelength shifter, *Journal of Synchrotron Radiation* 14 (4) (2007) 320–325.